Suppression of Nonsynchronous Vibration Through Intentional Aerodynamic and Structural Mistuning

Sina Stapelfeldt, Christoph Brandstetter

SUPPRESSION OF NON-SYNCHRONOUS-VIBRATION THROUGH INTENTIONAL AERODYNAMIC AND STRUCTURAL MISTUNING

Sina Stapelfeldt
Vibration University Technology Centre
Imperial College London
London, United Kingdom
Email: s.stapelfeldt@ic.ac.uk

Christoph Brandstetter*
Univ de Lyon, Ecole Centrale de Lyon, CNRS
Univ Claude Bernard Lyon 1, INSA Lyon, LMFA
UMR 5509, F-69134, ECULLY, France
Email: christoph.brandstetter@ec-lyon.fr

ABSTRACT

Non-synchronous vibrations (NSV) arising near the stall boundary of compressors are a recurring and potentially safety-critical problem in modern axial compressors and fans. Recent research has improved predictive capabilities and physical understanding of NSV but prevention measures are still lacking. This paper addresses this by systematically studying the influence of aerodynamic and structural mistuning on NSV. This is achieved by incorporating mistuning effects in a validated linear model, in which individual blade modes are modelled as single-degree of freedom mass oscillators coupled by a convected aerodynamic disturbance term. The results demonstrate that both structural and aerodynamic mistuning are effective. While structural mistuning improves stability by preventing aero-structure lock-in, aerodynamic mistuning, which locally reduces the tip blockage, attenuates the aerodynamic disturbance causing NSV. In the latter case, the circumferentially-averaged conditions are shown to be most influential, while the pattern plays a minor role. A combination of moderate aerodynamic and structural mistuning (1%) was also found to be effective. These findings are relevant for design decisions, demonstrating that small blade-to-blade variations can suppress NSV.

1 Introduction

Non-synchronous vibrations (NSV) are a major concern for aero-engine manufacturers because large vibration amplitudes can cause high cycle fatigue and damage components. In modern engines, a particular type of non-synchronous vibration is common in the compressor front stages. It typically occurs near stall and has shown to be caused by circumferentially propagating aerodynamic disturbances that lock in with the rotor's natural vibration modes.

The phenomenon has received increasing attention in recent years. This is undoubtedly driven by current design trends, such as higher aerodynamic blade loading and blade-integrated disks (blisks) with reduced mechanical damping, which increase the risk of aeroelastic instabilities. One frequently cited study of the topic links the excitation of structural vibration modes to so-called 'rotating instabilities', aerodynamic disturbances which propagate around the circumference, but offered few physical explanations regarding the physical mechanisms driving fluid-structure coupling [2]. The interpretation in this paper is misleading, and an interpretation of the measured data which is consistent with the latest understanding of NSV is possible [3].

Kielb et al. [4] provided a physical explanation of 'non-synchronous vibrations' in the front stages of a compressor rig, occurring at part-speed. The vibrations could be mistaken for flutter but parameters, such as reduced frequency, incidence angle and Mach number, were uncharacteristically high for flutter. In addition, the aeroelastic frequency had shifted noticeably from the in-vacuo frequency which is not common for turbomachinery blading, where the mass ratio is high. In this research NSV was linked to a suction side vortex and tip flow unsteadiness which locked in with a rotor vibration mode. This conceptual understanding has been reinforced by other studies, where in the majority of the cases vibrations were detected close to stall. NSV has been linked to 'spike-type' stall precursors, such as leading edge spillage and trailing edge back flow, and circumferentially travelling aerodynamic disturbances [5–8].

In an experimental study on a transonic research compressor, in the following referred to as the Darmstadt compressor, Brandstetter et al. [9] measured lock-in of a circumferentially propagating vortical disturbance with rotor vibrations in the first tor-

*Address all correspondence to this author.

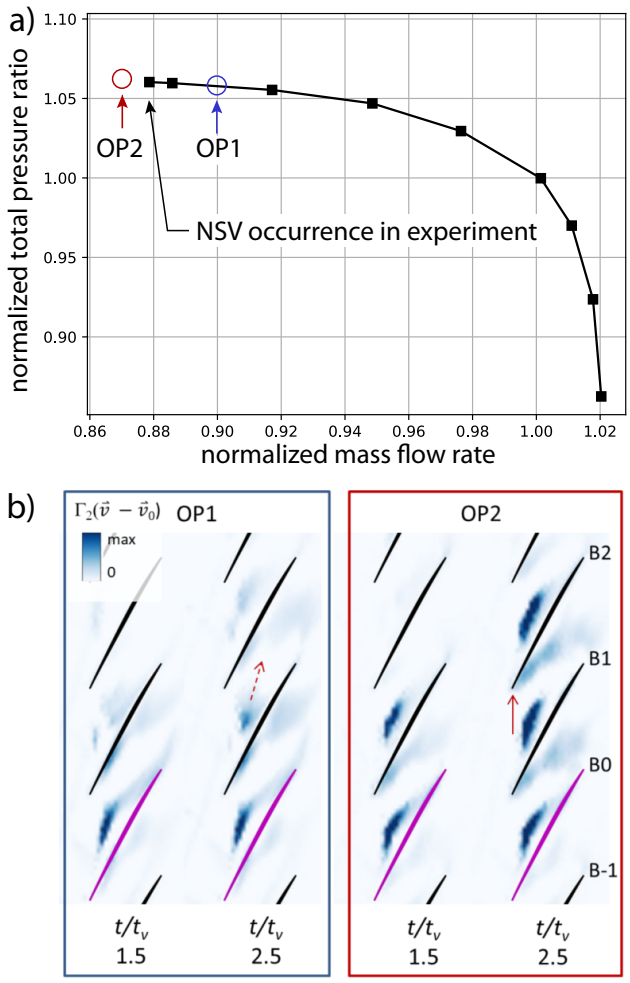

FIGURE 1: (a) Compressor characteristic and (b) aerodynamic disturbance propagation due to vibration of B0 at a stable (OP1) and unstable (OP2) operating point for different instants during one vibration cycle t_v, based on [1]

sional eigenmode. The vortical structures and wall-pressure signals detected were not unlike those identified in previous aerodynamic studies [10–12] and labelled 'radial vortices' or 'tornado vortices'.

To further investigate the lock-in between blade vibration and aerodynamic disturbance, Stapelfeldt and Brandstetter [1] performed numerical simulations at two operating points, one close to stall and one close to peak rotor pressure rise. The simulations proved that the aerodynamic forces and resulting blade deflections are driven by a vortical disturbance. At unstable conditions, this disturbance propagated mainly circumferentially (OP2), whereas at stable conditions (OP1) it propagated also axially out of the rotor domain as seen in Fig. 1. Since the aeroelastic system becomes unstable through the convection of vorticity, we refer to it as 'convective NSV'. The characteristics of this type of NSV are as follows:

- It occurs close to the stall boundary, but before rotating stall
- Prior to convective NSV, frequency spectra of unsteady pressure contain broad-band frequencies, which result from multi-wave number disturbances propagating at approximately 50% of the rotor speed in the direction opposing rotation (in the rotor frame of reference).
- At the onset of vibration, the aerodynamic disturbance locks in with the structural vibration and the broadband spectrum changes to a coherent aerodynamic disturbance with a distinct frequency peak.

Two important criteria must be fulfilled for it to occur:

- The mean aerodynamics must promote circumferential convection of vorticity, i.e. the passage must be blocked close to the casing to allow circumferential convection.
- The blade vibration must be able to shift the propagation velocity of the aerodynamic disturbance to create a coherent disturbance in resonance with the vibration pattern.

This description was later supported by numerical results from Moeller et al. [8] who performed full-circumference simulations of the 1.5-stage Darmstadt compressor with different tip clearances. They found that the experimentally detected radial vortices are formed by fluctuations of the shear layer between the tip leakage and main passage flow and NSV occurred when the rotor tip loss coefficient was high, i.e. the passage in the outer sections was blocked by tip leakage fluid, and the shear layer fluctuations travelled circumferentially. The convective nature of this type of NSV was also confirmed experimentally by Franke et al. [13] who demonstrated that with varying rotor speed or preswirl, i.e. with varying swirl velocity in the tip region, the nodal diameter of the aeroelastic instability changes. This delivered further experimental justification for the model developed in [1].

While significant amount of research has been dedicated to understanding and predicting NSV over the last twenty years, preventing it remains a challenge. A few studies showed that casing treatment slots, tip injections and non-axisymmetric casings were effective at delaying the onset of vibrations [14, 15]. However, a systematic study into mitigation measures has not been published.

One measure known to be successful at reducing vibrations is mistuning. This can be either structural, where the natural frequencies of individual blades around the circumference vary, or aerodynamic, with blade-to-blade variations in the (time-averaged) flow field. This has been extensively studied in the context of flutter and forced response, see for example References [16–18]

The aim of this paper is to demonstrate and explain the effectiveness of different types of mistuning (structural and aero-

dynamic) to prevent convective NSV. This will be achieved by incorporating mistuning in the model developed in Reference [1] and [19], which was previously validated against experimental measurements for the Darmstadt transonic compressor.

2 Model

2.1 Formulation

The model presented by [1] uses single-degree of freedom mass oscillators to represent blades on a rigid disk. In its simplest form, the individual blades are tuned and structurally uncoupled but aerodynamically coupled by a forcing term. In the case of convective NSV, the forcing is caused by a circumferentially propagating vorticity disturbance. The aerodynamic disturbance can be quantified as a superposition of the force induced directly by the blade vibration $F_v(t)$ and that caused by a circumferentially propagating vortical disturbance $F_a(t)$, which will also be referred to as the aerodynamic disturbance in the following. In References [1] and [19] this is laid out in detail. The equation of motion for the system of N_B blades is given by:

$$\ddot{\boldsymbol{\alpha}}(t) + D\dot{\boldsymbol{\alpha}}(t) + K\boldsymbol{\alpha}(t) = \boldsymbol{F_v}(t) + \boldsymbol{F_a}(t) \tag{1}$$

where $\boldsymbol{\alpha}$ is the vector of modal displacement and D and K are the diagonal damping and stiffness matrices respectively. Assuming harmonic oscillation of the N_B blades with frequency ω_v, constant amplitude and an interblade phase angle of $\sigma_v = 2\pi N_v/N_B$, the instantaneous amplitude α_n of Blade n is given by:

$$\alpha_n(t) = \hat{\alpha} e^{i(\omega_v t - n\sigma_v)} \tag{2}$$

Following the same approach as in [19], we will now derive an expression for the forces acting on one blade. The force due to vibration F_v is proportional to the blade deflection and can be expressed with the complex coefficient $\tilde{C}_v$:

$$F_v(t) = \tilde{C}_v \alpha(t) \tag{3}$$

The aerodynamic force $F_a(t)$ is dominated by the convection of vorticity. In the locked-in state, vorticity is generated at oscillating blades and convected with the flow to the trailing blades as seen in Fig. 1. The force F_a on any given blade is therefore a superposition of the forces generated by vortical disturbances from all preceding blades. We differentiate between the number of preceding blades N, which is the number of blades that contribute to the force on any given blade, and the number of blades in the circumference N_B. Since the disturbance can last several revolutions, N can be greater than N_B. The amplitude of the force is directly proportional to the amplitude of the disturbance, and for small blade deflections ($a < 1^\circ$), the amplitude of this disturbance is linearly dependent on the vibration amplitude [1]. We can therefore write the force acting on one blade, due to the vortical disturbances being emitted from the other blades as:

$$F_a(t) = \sum_{n=0}^{N-1} \tilde{C}_{a,n} \alpha_n(t) \tag{4}$$

where $n = 0$ is the first preceding blade, and $\tilde{C}_{a,n} = \hat{C}_{a,n} e^{i\phi_n}$ is the complex coefficient describing the force acting on one blade due to the vibration of preceding blade n. This is very similar to the aerodynamic influence coefficients used for flutter analysis but we will now derive an expression for $\tilde{C}_{a,n}$ in terms of a single aerodynamic force coefficient.

To find an expression for $\tilde{C}_{a,n}$ we take advantage of the fact that the contribution to the forcing from individual blades differ only in phase and amplitude. We can determine the phase of the disturbances from their convection speed, Ω_a^R and the frequency of blade vibration, ω_v, in the rotor frame of reference. The time taken by the disturbance to travel one pitch is given by:

$$T = -\frac{2\pi}{N_B \Omega_a^R} \tag{5}$$

For a vibration frequency ω_v, this transfers to an aerodynamic inter-blade phase angle:

$$\sigma_a = \omega_v T = -\frac{2\pi\omega_v}{N_B \Omega_a^R} \tag{6}$$

The amplitudes of the force coefficients will vary because the amplitude of a vortical disturbance decays while it travels around the circumference, as vorticity is not convected purely circumferentially but also axially out of the domain. We assume that the vortical disturbance decays exponentially with the number of pitches travelled. The amplitude of the disturbance caused by Blade n then scales as:

$$\hat{C}_{a,n} = \hat{C}_a^* e^{-nr_a} \tag{7}$$

where $\tilde{C}_a^* = \tilde{C}_{a,0}$ is the complex force coefficient describing the force exerted on a blade due to the oscillation of the immediately preceding blade. This is the same as the force exerted by an oscillating blade on its trailing blade. It is calibrated using CFD simulations by measuring the force exerted on Blade B1 through oscillation of Blade B0, following the numbering convention in Fig 1.

By substituting the expression for the vibration inter-blade phase angle (2), the amplitude scaling factor (7), and the aerodynamic inter-blade phase angle (6) into Eq. 4, the aerodynamic forcing on a given blade due to the vibration of preceding N blades can be written as:

$$F_a(t) = \sum_{n=0}^{N-1} \tilde{C}_a^* e^{-nr_a} e^{-i(n\sigma_v + n\sigma_a)} a e^{i\omega_v t} \tag{8}$$

This expression for the force due to the aerodynamic disturbance, and the expression for the force due to blade vibration (3), can be substituted into the equation of motion 1, which now fully describes the aeroelastic system.

As was demonstrated in [1] the model coefficients, namely the propagation speed, the forcing coefficients and the decay

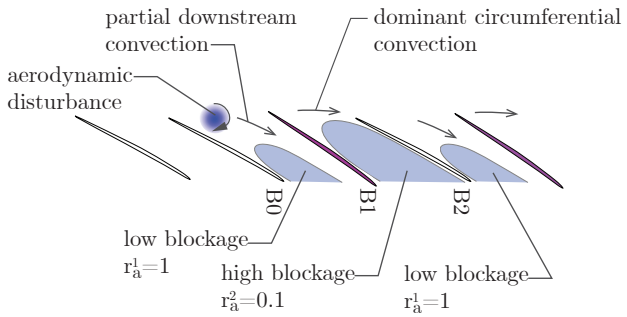

FIGURE 2: Schematic of disturbance propagation in a blade row with aerodynamic mistuning, for example alternating blade stagger angle, blade sweep or tip clearance causing inhomogeneous tip blockage.

rate of disturbances, can be calibrated using unsteady URANS-simulations in a multi-passage setup with one oscillating blade. It was shown, that at the operating point close to stall (OP2 in Fig. 1), where the vorticity convection was primarily in the circumferential direction, the disturbance amplitude remained almost constant in the circumferential direction, which could be modelled by a low decay rate r_a. Away from stall (OP1 in Fig. 1), a large proportion of vorticity convected axially out of the domain leading to a decay in amplitude of the disturbance in the leading edge plane. Hence, the decay rate r_a is high for OP1. At the same time, the simulations showed that neither convection speed nor forcing coefficients changed noticeably between operating points [1].

2.2 Aerodynamic Mistuning

To introduce aerodynamic mistuning, we assume that there are different types of blades with different flow fields but we keep the force coefficients constant. This is a reasonable assumption since they were found to vary little between operating points and have little influence on stability [1, 19]. In the model described above this is represented by a modified attenuation coefficient $r_{a,n}$, which depends on the blade as illustrated in Fig. 2. Assuming that a disturbance travels through different passages with constant speed, the scaling coefficient for the aerodynamic force contribution from Blade n becomes:

$$\begin{aligned}\hat{C}_{a,n} &= \hat{C}_a^* \Pi^n e^{-r_{a,n}} \\ &= \hat{C}_a^* e^{\Sigma^n - r_{a,n}}\end{aligned} \tag{9}$$

which recovers Eq. 7 for a constant r_a. For an alternating mistuning pattern with attenuation coefficients r_a^1 and r_a^2:

$$\hat{C}_{a,n} = \hat{C}_a^* e^{-N_1 r_a^1 - N_2 r_a^2} \tag{10}$$

where N_1 and N_2 are the number of blades between preceding Blade n and Blade 0 with r_a^1 and r_a^2 respectively.

For an arbitrary pattern, the expression for aerodynamic forcing then becomes:

$$F_a(t) = \sum_{n=0}^{N-1} \tilde{C}_a^* \hat{\alpha} e^{i\omega_v t} e^{-\Sigma^n r_{a,n}} e^{-i(n\sigma_v + n\sigma_a)} \tag{11}$$

Substituting this expression for the force resulting from the accumulated aerodynamic disturbance and the force resulting from vibration of the blade itself into the equation of motion 1 results in a linear system, the stability of which can be analysed using eigenvalue analysis.

Various patterns with blade individual attenuation coefficients varying between r_a^1 and r_a^2 are modelled as follows:

$$r_{a,n} = (A_n + 0.5) r_a^1 + (0.5 - A_n) r_a^2 \tag{12}$$

where A_n is the mistuning coefficient applied to Blade n. This defines the patterns (circumferential arrangement) which are listed in the Appendix.

2.3 Structural mistuning

Structural mistuning is incorporated into the model by considering a varying blade stiffness in the coupled model. According to the patterns of A_n from the Appendix, the stiffness matrix K in eq.1 is assembled as follows:

$$K_{n,n} = (\omega_v (1 + A_{smt} A_n))^2 \tag{13}$$

with ω_v being the reference eigenfrequency of the blade and A_{smt} representing the structural mistuning amplitude. The coupled system is integrated over time and the vibration pattern Fourier-transformed to derive the initial transient evolution of each nodal diameter amplitude. An exponential fit is applied to derive the damping coefficient ζ for every N_v. The time-marching implementation was validated against the eigenvalue analysis presented for the tuned case.

2.4 Parameter choice

The model was validated against numerical and experimental results in [1, 19]. To study the effects of mistuning on a representative case, the force coefficients $\tilde{C}_a^*$, $\tilde{C}_v$ as well as vibration frequency ω_v^R and number of blades N_B are set to those of the transonic research compressor investigated in [1]. A compressor characteristic and two operating points of interest are sketched in Fig. 1a. As typical NSV, the compressor is unstable at the operating point close to stall, where the passage is blocked in the tip region and the vorticity disturbance convects circumferentially with little decay as illustrated in Fig. 1b. At a slightly higher mass flow (OP1), tip blockage is reduced allowing vorticity to convect axially and the rotor is stable. This is consistent with experiments where NSV occurred between OP1 and OP2 [9]. The parameters for the two operating points are listed in Table 1.

Previous studies, published in [19], showed that the influence of force coefficients, $\tilde{C}_a$ and $\tilde{C}_v$, on aeroelastic stability is

	OP1	OP2
$\tilde{C}_a^* \hat{\alpha}$	$12e^{i(-0.5\pi)}$	$12e^{i(-0.375\pi)}$
$\tilde{C}_v \hat{\alpha}$	$50e^{i(0.25\pi)}$	$50e^{i(0.25\pi)}$
N_B	21	21
ω_v^R/Ω_r	5.81	5.81
r_a	1.0	0.075
Ω_a^R/Ω_r	-0.44	-0.44

TABLE 1: Model coefficients and parameters used for the stable (OP1) and unstable (OP2) operating points

small and that the propagation speed Ω_a^R and the circumferential decay rate of the aerodynamic disturbance r_a drive the instability. These two parameters are determined by changes in the swirl velocity (rotor speed) and tip blockage (operating point) respectively. Hence, the present investigation keeps the force coefficients constant but varies the decay rate r_a and the propagation speed Ω_a^R to assess the effect of mistuning over a range of conditions.

3 Results

3.1 Structural mistuning

To demonstrate the effectiveness of structural mistuning against NSV, a range of frequency mistuning patterns is tested using the model described above. The patterns are shown in Fig 3, and values are listed in the Appendix. They were chosen to test a range of arrangements: alternating (P1), random (P2), linear (P3) and sinusoidal variations of two different wave lengths (P4 and P5). Patterns P2-P5 have the same blade-individual frequency, only their circumferential arrangement differs. In the case of bladed disks this allows the assessment of intentional arrangement of blades with random manufacturing tolerance.

Each pattern is tested with different mistuning amplitudes, defined as the fractional frequency deviation between the maximum and nominal blade frequency:

$$A_{smt} = \frac{\omega_{v,max}^R - \omega_{v,min}^R}{\omega_{v,nominal}^R} \tag{14}$$

To begin, the influence of mistuning is studied at the experimentally and numerically tested unstable operating point, OP2. A damping curve for 1% mistuning amplitude in Pattern 2 is compared to the tuned case in Fig. 4 as an example. Without mistuning, only nodal diameter $N_v = 8$ is unstable, which agrees with the experiment [9] where NSV was observed for $N_v = 8$. The sharp drop in aero-damping is caused by a resonance between the convected aerodynamic disturbance and the blade vibration. At resonance, the frequency of the aerodynamic (or acoustic) disturbance and its inter-blade phase angle coincide with that of the vibration mode, i.e. the following condition is fulfilled:

$$\omega_v^R = \Omega_a^R N_a \quad , \quad \sigma_a = \sigma_v \tag{15}$$

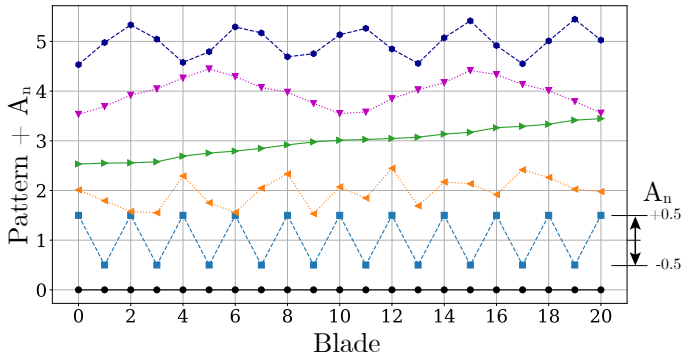

FIGURE 3: Frequency mistuning patterns

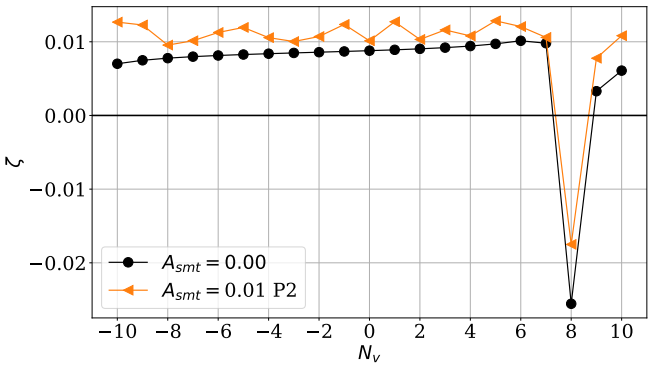

FIGURE 4: Aerodynamic damping versus nodal diameter for different frequency mistuning patterns with 1% mistuning amplitude, $\Omega_a^R/\Omega_r = -0.44$

A similar behaviour, with sudden changes in aero-damping at resonance, is typical for cases of acoustic resonance. When mistuning is introduced, $N_v = 8$ remains the most critical mode but aero-damping has increased from approximately -2.5% to -1.75%. As the natural frequencies differ between individual blades, there is no constant phase-lag between blades, which results in aero-damping fluctuations between nodal-diameters in the tuned range as seen in Fig. 4. However, it is clear that mistuning increases the average aero-damping compared to the tuned case.

Since the design objective is to stabilise the compressor across the whole operating range, the model parameters are now varied to represent changes in operating condition and the minimum aerodynamic damping for each condition is extracted. Since only operating points with a low decay rate are unstable, the following analysis will concentrate on a variation of propagation speed while other model parameters are kept constant at values representative of the unstable operating point (OP2).

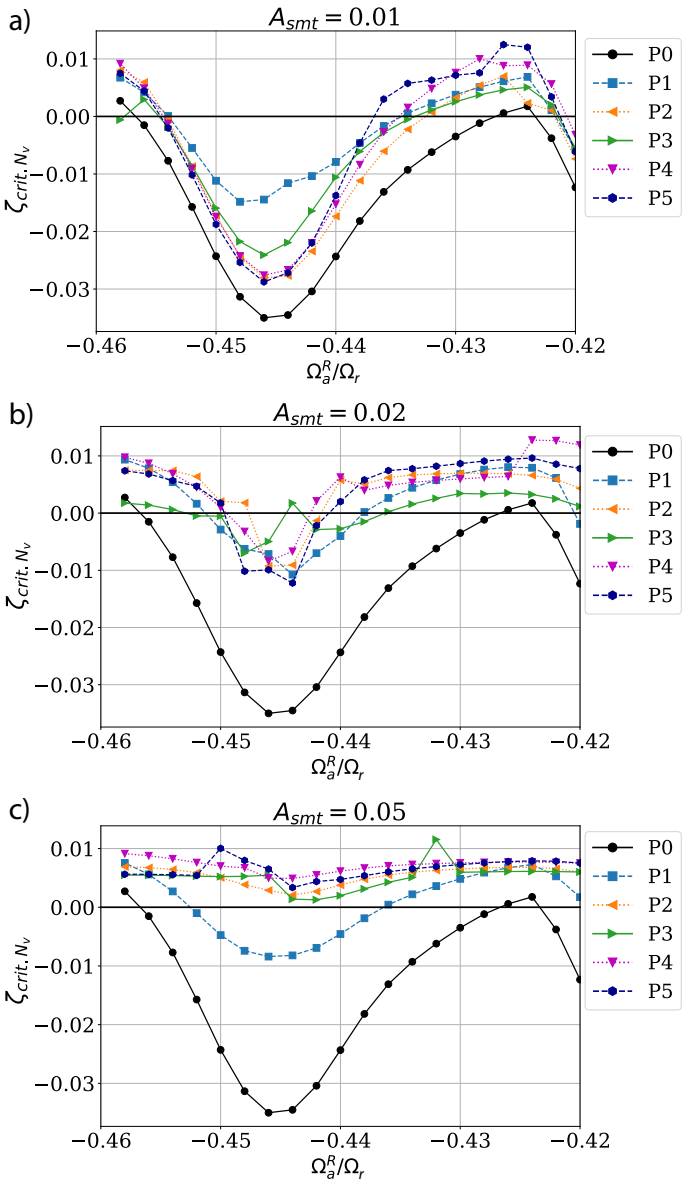

FIGURE 5: Variation of minimum aerodynamic damping with propagation speed for different structural mistuning patterns, a) 1% mistuning, b) 2% mistuning, c) 5% mistuning

Figure 5 shows the damping in the critical (most unstable) nodal diameter, ζ_{crit,N_v}, as a function of convective speed for different mistuning amplitudes. For the tuned case (P0), aero-damping is smallest at the resonance condition $\Omega_a^R \approx -0.447$, where the free phase-speed of the aerodynamic disturbances matches that of the structural vibration. As shown in [1], the system can develop a single aeroelastic frequency through adaptation of the nodal diameter and, to a smaller extent, propagation speed. Therefore, lock-in can also occur when the phase-speed of the free aerodynamic disturbance deviates from that of the vibration but the magnitude of aerodamping changes. This can be seen in Fig. 5, where for the tuned case lock-in occurs over the whole range of free propagation speeds. Between $\Omega_a^R = -0.460$ and $\Omega_a^R = -0.425$ the aerodynamic wave number is constant at $N_a = 13$ but the magnitude of aero-damping varies with propagation speed. At a higher free propagation speed the systems locks in to wave number $N_a = 14$ ($N_v = 7$) [1]. All mistuning patterns and amplitudes improve stability compared to the tuned case. However, the patterns behave differently as mistuning amplitude is increased.

For 1% mistuning, shown in Fig. 5(a), aero-damping increases but the shape of the curve does not change significantly. The alternating pattern (P1) is the most effective and more than halves the negative aero-damping at resonance condition. Off-resonance between $-0.435 < \Omega_a^R < -0.420$, all patterns stabilise the rotor.

Figure 5 (b) shows that doubling the mistuning amplitude has a large effect. The stable range is extended significantly but a small unstable range remains near resonance for all mistuning patterns. There is no longer a distinct advantage from the alternating pattern compared to the others. Increasing the mistuning amplitude to 5% (Fig. 5 (c)) completely stabilises the rotor for four patterns. In this case, the alternating pattern is the only one that remains unstable near resonance.

A shift in the location of minimum aero-damping can also be seen for some patterns in Figure 5 (b) and (c). This is caused by the frequency of the aeroelastic system shifting from its tuned frequency when the mistuning amplitude is sufficiently high.

For a better comparison of patterns and amplitudes, the minimum aero-damping over the range of convection speeds is plotted in Fig. 6. It shows that the effect of the alternating pattern (P1) does not vary much with amplitude, whereas varying the mistuning amplitude for the other patterns results in large changes (>100%) in aero-damping. As mentioned above, Patterns P2-P5 are all stable with 5% mistuning.

3.2 Aerodynamic mistuning

Aerodynamic mistuning is modelled by changing the decay rate as described above. In the first experiment, the decay rate is doubled over part of the circumference, from $r_a^1 = 0.075$ on half of the blades to $r_a^2 = 0.15$ on the other half, and various patterns are tested. Pattern P0 represents the tuned case with an average decay rate, $\bar{r}_a$=0.1125 (see Eq. 12). As seen in Fig. 7, attenuating the disturbance more over half of the circumference reduces the aero damping magnitude of the critical (most unstable) nodal diameter by approximately 50% compared to the tuned reference case. The influence of the pattern is marginal and the aero-damping is similar to that of the tuned case with an increased decay rate (P0). Fig. 8 shows the same curves but the

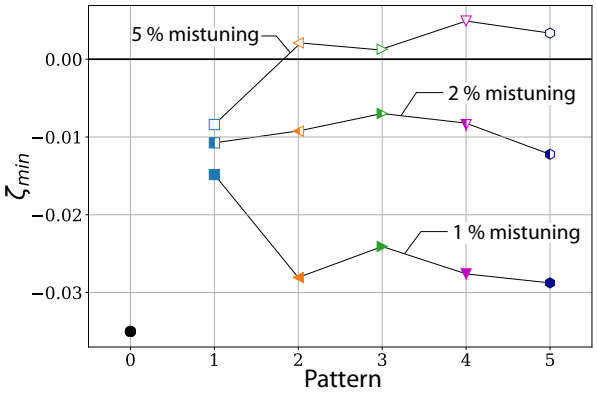

FIGURE 6: Minimum aero-damping for different mistuning patterns and amplitudes. Full symbols 1%, half symbols 2%, empty symbols 5% structural mistuning amplitude

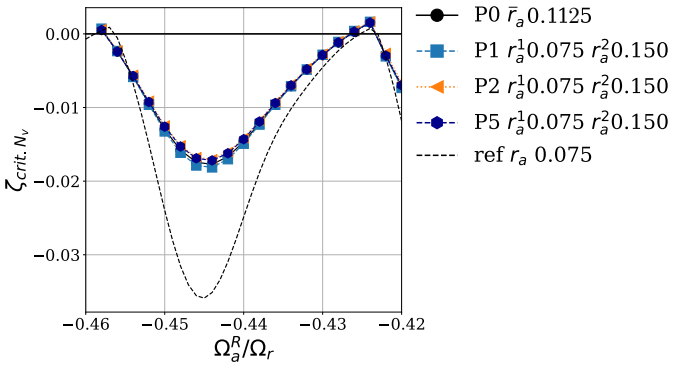

FIGURE 7: Variation of minimum aerodynamic damping with propagation speed for different aerodynamic mistuning patterns with $r_a^1 = 0.075$ and $r_a^2 = 0.15$. Tuned case $r_a = 0.075$.

decay rate over half of the blades has been increased. From a decay rate of $r_a^2 = 0.45$ the system becomes stable for Pattern P2. The other patterns remain marginally unstable at this decay rate but at $r_a^2 = 1.0$, corresponding to OP1, all patterns are stable.

Combined aero-structural mistuning

To assess the combined benefits of aerodynamic and structural mistuning, we choose the random structural pattern P2, which behaved similarly to Patterns P3-P5 and was completely stable with 5% mistuning amplitude, and vary aerodynamic mistuning. As before, the other model parameters are fixed at those for the unstable operating point, OP2.

The similar behaviour of the different aerodynamic mistuning patterns suggests that stability is not driven by local aerodynamic effects but by circumferentially averaged conditions. We

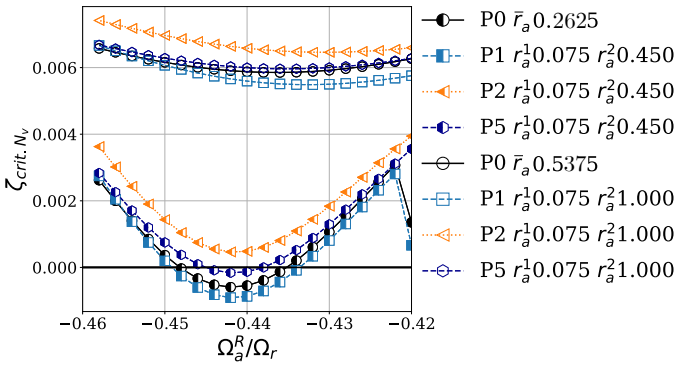

FIGURE 8: Variation of minimum aerodynamic damping with propagation speed for different aerodynamic mistuning patterns with $r_a^1 = 0.075$ and $r_a^2 = 0.45$ and $r_a^2 = 1.0$. Tuned case P0

therefore define an average decay rate for patterns with two blade sets to define the aero-mistuning amplitude:

$$\bar{r}_a = \frac{r_a^1 + r_a^2}{2} \tag{16}$$

To allow a more intuitive interpretation of this decay coefficient, we express it in terms of half-life of the aerodynamic disturbance, given by $t_h = log2/\bar{r}_a$.

Figure 9 plots the minimum aero-damping across the range $-0.46 < \Omega_a^R < -0.42$ as the average decay rate is varied for three levels of structural mistuning. Without structural mistuning, aerodynamic damping depends linearly on the half-life of the aerodynamic disturbance and the system becomes stable for an average $\bar{r_a} = 0.3$, or half-life $t_h = 2.3$ passages. When the decay of the aerodynamic disturbance is lower, the linear model predicts instability. Structural mistuning lowers the critical decay rate, or raises the critical half-life as seen by the orange curves in Fig. 9. For 1% structural mistuning, the system becomes stable at $\bar{r_a} = 0.14$ ($t_h = 5$), while for higher levels of structural mistuning, the aerodynamic effects diminish and the rotor is stable.

3.3 Casing Treatments or aerodynamic stator mistuning

The mitigation measures assessed so far have concerned circumferential variations in the rotor. It was shown in several investigations that the application of different types of casing treatments or eccentricity extends the operating range and delays the onset of NSV [14, 15, 20]. Both half-heart shaped axial slots above the leading edge and a recirculating tip injection are highly effective [21]. Here it was shown that non-synchronous activity related to the circumferential propagation of vorticity disturbances are significantly reduced. This lets us conclude, that the decay rate of disturbances is effectively increased through the casing treatment or reduced tip clearance. In the context of the

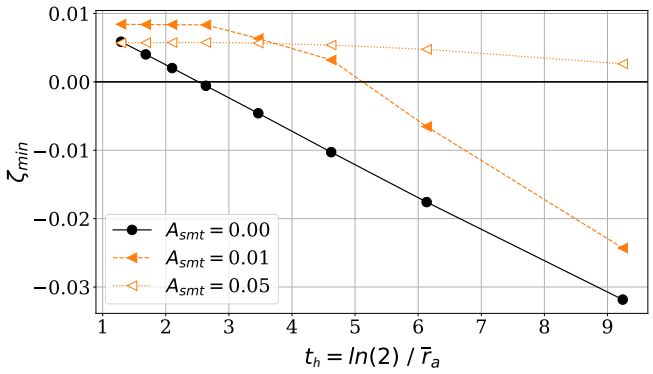

FIGURE 9: Variation of minimum aerodynamic damping with average decay coefficient for three levels of structural mistuning in Pattern 2

results presented above a possible modelling approach is a temporal variation of the decay coefficient r_a as a function of the circumference. Results of the time marching model show the same tendency as seen in Fig. 9, with the stability enhancement proportional to the circumferential extension of the casing treatment. Quantification of the underlying parameters requires further studies.

4 Discussion

A number of general results emerged from the mistuning study which will now be summarised and discussed.

Frequency mistuning was found to be effective at increasing aero-damping but only at relatively large mistuning amplitudes. The variations necessary to stabilise the rotor under investigation were approximately 5%. This is well outside the range of manufacturing tolerances and the required amplitudes may cause problems of forced response. The pattern was found to play a role, with particularly the alternating pattern performing comparatively badly at large mistuning amplitudes. Furthermore, excessive structural mistuning is known to be detrimental for forced response behaviour.

Aerodynamic mistuning was also found to successfully suppress convective NSV. The most influential factor is the average decay rate of the aerodynamic disturbance. Its circumferential distribution played a negligible role. In a compressor, the change in decay rate is achieved by locally reducing the tip blockage to reduce the component of disturbance being convected in the circumferential direction. The change in decay rate necessary to stabilise the blade (from $r_a = 0.075$ to 0.30 without structural mistuning) appears large but it is helpful to put it into context by considering the changes in decay rate across a compressor operating range. Previous studies [1] measured a decay rate close to 1 at a stable operating point close to rotor peak pressure rise, compared to 0.075 at NSV conditions (see Tab. 1). This represents a more than ten-fold increase in decay rate between two close operating points. In a similar investigation, the change in tip loss coefficient between the stable and unstable operating point was found to be of the order of 0.05 [8]. Taking the tip loss coefficient as a measure of tip blockage and circumferential transport, the mistuning results imply that *locally* reducing tip loss coefficient by *less* than 5% is effective at mitigating NSV. To quantify this further, the relationship between r_a and an aerodynamic measure, such as tip loss coefficient, needs to be further investigated.

As **casing treatments** are known to reduce disturbances occurring in the leading edge area close to the casing, the experimental findings from [14, 21] support the findings presented here. For the compressor under investigation, the application of 18 flow recirculating nozzles significantly shifted the stability limit altering the average compressor performance. Reduction of the number of nozzles reduced the stabilizing effect in proportion. The results presented here indicate that such a feature to attenuate circumferential propagation of disturbances does not necessarily be homogeneous around the circumference, providing enormous design potential.

Applicability to other compressors and fans Although the model parameters studied in this paper were chosen to be representative of the Darmstadt compressor, the conclusions drawn are considered to be general for two reasons; Firstly, they are based on general trends observed during sweeps of the non-dimensional parameters known to be most influential to NSV. The parameters kept fixed in this study, i.e. the force coefficients, have a minor effect on stability [19]. Secondly, in the authors' experience, the values chosen do not appear to vary significantly from machine to machine, including HPC compressors [1] and low-speed fans [22]. Propagation speeds reported in literature, for example, are around 50% rotor speed [2, 4, 22–25]. The most unstable speed will change with the ratio of natural frequency to propagation speed, as dictated by the resonance condition, but this does not affect the trends discussed here. Similarly, the decay rate of the compressor was found to be comparable to other machines. The model with the coefficients shown here, was able to able correctly predict the unstable nodal diameter for a number of cases from literature, listed in Table 2.

5 Conclusion

A reduced order mistuning model to predict compressor non-synchronous vibrations, which occur near the stall boundary and are caused by the circumferential convection of aerodynamic disturbances, was presented. The model was used to investigate the influence of different types of mistuning on aeroelastic stability. It was demonstrated that comparatively large structural mistuning amplitudes (5%) are necessary to stabilise the system

and the circumferential arrangements of the blades plays a role. With aerodynamic mistuning, on the other hand, the stability is determined by the circumferentially averaged conditions and the influence of the pattern is negligible. The aerodynamic mistuning can be introduced through variations in the rotor geometry. This is the first time that mistuning has been systematically analysed in this context and the results agree with experimental observations on a high speed compressor, where casing treatments were found to delay the onset of vibrations. The model can be calibrated from reduced-domain CFD simulations and is therefore a fast and cost-effective means of assessing the risk of NSV and mitigation measures, such as deliberate arrangement of blades with intentional and unintentional manufacturing differences, in engine design.

	N_B	Ω_a^R/Ω_r	ω_v/Ω_r	$\sigma_{v,exp}$	$N_{v,exp}$
[2] Baumgartner et al. **trans. multist. HPC**	27	−0.36	7.56	80°	6
[23] Kameier & Neise **low speed axial fan**	24	−0.6	22.2	165°	11
[9] Brandstetter et al. **trans. sing. stg. HPC**	21	−0.44	5.8	137°	8
[22] Rodrigues et al. **transonic fan**	16	−0.42	5.46	67.5°	3

TABLE 2: NSV cases from literature successfully captured by the model

ACKNOWLEDGMENT

The authors would like to thank Roque Corral, Bob Kielb, Ken Hall, Xavier Ottavy and Nick Cumpsty for useful discussions which helped to motivate this research.

The presented research was supported through Clean Sky 2 Joint Undertaking (JU), project CATANA under grant agreement N°864719. The JU receives support from the European Union's Horizon 2020 research and innovation programme and the Clean Sky 2 JU members other than the Union. This publication reflects only the author's view and the JU is not responsible for any use that may be made of the information it contains. The authors also thank EPSRC for the support under the Prosperity Partnership Grant "Cornerstone: Mechanical Engineering Science to Enable Aero Propulsion Futures", Grant Ref: EP/R004951/1.

NOMENCLATURE

A_n	Mistuning coefficient (Table 3)
A_{smt}	Struct. mistuning amplitude
$\tilde{C}_a^*$	Force Coefficient
F	Unsteady force
N	Number of blades modelled
N_B	Number of rotor blades
N_a	Aerodynamic wave number
N_v	Structural nodal diameter
OP	Operating Point
P0-P5	Mistuning Pattern (Table 3)
r_a	Aerodynamic disturbance decay rate
r_a^1, r_a^2	Decay rates for aerodynamic mistuning
t	Time
t_h	Half life
α	Modal displacement
$\hat{\alpha}$	Modal displacement amplitude
ζ	Aerodynamic damping ratio
ω	Angular vibration frequency
Ω	Angular velocity
σ	Inter-blade phase angle
Subscripts	
a	aerodynamic disturbance
v	structural vibration
r	rotor
Superscripts	
R	Relative to rotor frame of reference
S	Relative to stator frame of reference

REFERENCES

[1] Stapelfeldt, S., and Brandstetter, C., 2020. "Non-synchronous Vibration in Axial Compressors: Lock-in Mechanism and Semi-Analytical Model". *J. Sound Vib.,* **488**, p. 115649.

[2] Baumgartner, M., Kameier, F., and Hourmouziadis, J., 1995. "Non-engine order blade vibration in a high pressure compressor". In Twelfth international symposium on airbreathing engines, Melbourne, Australia.

[3] Brandstetter, C., Ottavy, X., Paoletti, B., and Stapelfeldt, S., 2021. "Interpretation of Stall Precursor Signatures". *Journal of Turbomachinery,* **143**(12), 07. 121011.

[4] Kielb, R. E., Barter, J. W., Thomas, J. P., and Hall, K. C., 2003. "Blade excitation by aerodynamic instabilities: A compressor blade study". In ASME Turbo Expo 2003, Atlanta, GA, June 16-19, pp. 399–406.

[5] Vo, H. D., Tan, C. S., and Greitzer, E. M., 2008. "Criteria for spike initiated rotating stall". *J. Turbomach.,* **130**(1), pp. 11023–11029.

[6] Vo, H. D., 2010. "Role of tip clearance flow in rotating instabilities and nonsynchronous vibrations". *J. Propul. Power,* **26**(3), pp. 556–561.

[7] Im, H., and Zha, G., 2014. "Investigation of flow instability mechanism causing compressor rotor-blade nonsynchronous vibration". *AIAA journal,* **52**(9), pp. 2019–2031.

[8] Möller, D., and Schiffer, H.-P., 2021. "On the Mechanism of Spike Stall Inception and Near Stall Nonsynchronous Vibration in an Axial Compressor". *Journal of Engineering for Gas Turbines and Power,* **143**(2), 01. 021007.

[9] Brandstetter, C., Juengst, M., and Schiffer, H.-P., 2018. "Measurements of Radial Vortices, Spill Forward, and Vortex Breakdown in a Transonic Compressor". *J. Turbomach.,* **140**(6), pp. 061004–061004–14.

[10] Inoue, M., Kuroumaru, M., Tanino, T., and Furukawa, M., 2000. "Propagation of multiple short-length-scale stall cells in an axial compressor rotor". *J. Turbomach.,* **122**(1), pp. 45–54.

[11] Young, A., Day, I., and Pullan, G., 2013. "Stall warning by blade pressure signature analysis". *J. Turbomach.,* **135**(1), p. 11033.

[12] Pullan, G., Young, A. M., Day, I. J., Greitzer, E. M., and Spakovszky, Z. S., 2015. "Origins and structure of spike-type rotating stall". *J. Turbomach.,* **137**(5), pp. 51007–51011.

[13] Franke, D., Jüngst, M., Möller, D., Schiffer, H.-P., and Giersch, T., 2020. "Influence of Pre-Swirl, Rotor Speed and Blade Count on Aeroelastic Coupling Mechanisms During Stall Inception of a Transonic Compressor". In ASME Turbo Expo: Power for Land, Sea, and Air, Vol. Volume 10A: Structures and Dynamics. V10AT24A015.

[14] Brandstetter, C., 2016. "Aerodynamische Stabilisierung transsonischer Axialverdichter - Eine experimentelle Untersuchung der Blattspitzenströmung unter dem Einfluss von Gehäusestrukturierungen". PhD thesis, TU Darmstadt, Aachen, May.

[15] Möller, D., Jüngst, M., Schiffer, H.-P., Giersch, T., and Heinichen, F., 2018. "Influence of rotor tip blockage on near stall blade vibrations in an axial compressor rig". *Journal of Turbomachinery,* **140**(2).

[16] Kaza, K. R. V., and Kielb, R. E., 1982. "Flutter and response of a mistuned cascade in incompressible flow". *AIAA Journal,* **20**(8), pp. 1120–1127.

[17] Beirow, B., Giersch, T., Kühhorn, A., and Nipkau, J., 2014. "Forced Response Analysis of a Mistuned Compressor Blisk". *Journal of Engineering for Gas Turbines and Power,* **136**(6), 02. 062507.

[18] Besem, F. M., Kielb, R. E., and Key, N. L., 2016. "Forced response sensitivity of a mistuned rotor from an embedded compressor stage". *Journal of Turbomachinery,* **138**(3).

[19] Brandstetter, C., and Stapelfeldt, S., 2021. "Analysis of a linear model for non-synchronous vibrations near stall". *International Journal of Turbomachinery, Propulsion and Power,* **6**(3).

[20] Jüngst, M., Franke, D., Schiffer, H.-P., and Giersch, T., 2018. "Aeroelastic effects in a transonic compressor with nonaxisymmetric tip clearance". In Global Power and Propulsion Society Forum 18, Montreal, 7th-9th May 2018.

[21] Brandstetter, C., Wartzek, F., Werner, J., Schiffer, H.-P., and Heinichen, F., 2016. "Unsteady measurements of periodic effects in a transonic compressor with casing treatments". *J. Turbomach.,* **138**(5), pp. 51007–51009.

[22] Rodrigues, M., Soulat, L., Paoletti, B., Ottavy, X., and Brandstetter, C., 2021. "Aerodynamic Investigation of a Composite Low-Speed Fan for UHBR Application". *Journal of Turbomachinery,* **143**(10), 05. 101004.

[23] Kameier, F., and Neise, W., 1997. "Rotating blade flow instability as a source of noise in axial turbomachines". *J. Sound Vib.,* **203**(5), pp. 833–853.

[24] Thomassin, J., Vo, H. D., and Mureithi, N. W., 2011. "The tip clearance flow resonance behind axial compressor non-synchronous vibration". *J. Turbomach.,* **133**(4), p. 041030.

[25] Dodds, J., and Vahdati, M., 2015. "Rotating Stall Observations in a High Speed Compressor—Part I: Experimental Study". *J. Turbomach.,* **137**(5), pp. 51002–51010.

Appendix

Blade	P0 ref	P1 altern	P2 random	P3 sort	P4	P5
0	0.0	0.5	0.010	9	9	9
1	0.0	-0.5	-0.206	3	13	20
2	0.0	0.5	-0.422	6	16	8
3	0.0	-0.5	-0.449	2	7	7
4	0.0	0.5	0.292	13	18	2
5	0.0	-0.5	-0.247	5	12	1
6	0.0	0.5	-0.442	1	4	4
7	0.0	-0.5	0.046	11	10	14
8	0.0	0.5	0.333	16	20	13
9	0.0	-0.5	-0.467	20	5	5
10	0.0	0.5	0.072	0	3	15
11	0.0	-0.5	-0.152	19	2	18
12	0.0	0.5	0.446	7	11	11
13	0.0	-0.5	-0.308	10	19	6
14	0.0	0.5	0.171	15	14	10
15	0.0	-0.5	0.135	14	17	17
16	0.0	0.5	-0.082	18	8	16
17	0.0	-0.5	0.415	4	15	3
18	0.0	0.5	0.263	8	0	0
19	0.0	-0.5	0.026	17	1	12
20	0.0	0.5	-0.022	12	6	19

TABLE 3: Mistuning Patterns, coefficients A_n for Pattern P1-P2, P3-P5 indicating blade index of permutations of Pattern 2